JOURNAL OF GEOPHYSICAL RESEARCH, VOL. 113, C05S94, doi:10.1029/2007JC004181, 2008

Click Here for Full Article

Evaluation of AMSR-E snow depth product over East Antarctic sea ice using in situ measurements and aerial photography

Anthony P. Worby,[1] Thorsten Markus,[2] Adam D. Steer,[1] Victoria I. Lytle,[3] and Robert A. Massom[1]

Received 22 February 2007; revised 1 August 2007; accepted 24 September 2007; published 23 May 2008.

[1] The Antarctic Remote Ice Sensing Experiment (ARISE) was conducted in the East Antarctic sea ice zone during September–October 2003. A key objective of this program was the acquisition of in situ measurements suitable for evaluating the EOS Aqua Advanced Microwave Scanning Radiometer (AMSR-E) snow depth product. A strategy is presented for comparing snow thickness measurements over spatial scales ranging from point measurements to satellite pixels. In situ measurements of snow thickness were taken across eight Lagrangian grid cells defined and tracked using an array of drifting buoys. These data are coupled with ice-type analyses from digital aerial photographs to calculate area-averaged snow thicknesses that are compared with the AMSR-E derived snow thickness product. The results show considerable underestimates of the AMSR-E snow depths for rough sea ice by a factor of 2.3. We investigate the impact of underlying sea ice roughness on snow depth retrievals and conclude that in situ measurements of snow thickness underrepresent snow depth over rough ice, which is then not adequately accounted for in the development of the algorithm coefficients.

Citation: Worby, A. P., T. Markus, A. D. Steer, V. I. Lytle, and R. A. Massom (2008), Evaluation of AMSR-E snow depth product over East Antarctic sea ice using in situ measurements and aerial photography, *J. Geophys. Res.*, *113*, C05S94, doi:10.1029/2007JC004181.

1. Introduction

[2] The depth of snow on sea ice is important for estimating surface albedo, the conductive heat flux between the ocean and atmosphere, and the fresh water flux to the ocean [*Massom et al.*, 2001]. It is also a critical parameter necessary for the accurate interpretation of satellite laser and radar altimeter measurements for determining sea ice thickness [e.g., *Kwok et al.*, 2004, 2006; *Wingham et al.*, 2006]. It is only recently that it has been possible to estimate this important parameter routinely on a regional scale, using new satellite remote sensing techniques.

[3] Snow depth on sea ice is a standard product of the EOS Aqua Advanced Microwave Scanning Radiometer (AMSR-E) instrument. This represents an average over an area of about 25 × 25 km^2, gridded to a 12.5 × 12.5 km^2 polar stereographic grid [*Comiso et al.*, 2003]. The algorithm was developed using a comparison of in situ snow depth measurements with DMSP Special Sensor Microwave/Imager (SSM/I) brightness temperatures (TB) of Southern Ocean sea ice [*Markus and Cavalieri*, 1998], however it has not been adequately validated over Antarctic sea ice on an individual pixel scale. The algorithm is similar to the snow on land algorithms and makes use of the difference in scattering by snow between the 19- and 37-GHz frequencies at vertical polarization. Sea ice has a high emissivity (about 0.95) for both the 19- and 37-GHz channels. Thus the difference between brightness temperatures for these two channels (TB_{19V} and TB_{37V}, respectively) is close to zero for snow-free sea ice. With increasing snow depth, the radiation emitted by the sea ice is increasingly scattered. The attenuation through scattering is greater at 37 GHz than at 19 GHz, so that increasing snow depth results in relatively greater brightness temperatures at 19 GHz compared to 37 GHz [e.g., *Chang et al.*, 1987; *Markus and Cavalieri*, 1998].

[4] While the accuracy of AMSR-E snow depth retrievals is still uncertain, regional snow depth distributions on monthly timescales agree well with in situ observations, at least over relatively level ice [*Markus and Cavalieri*, 1998]. Current limitations of the AMSR-E snow depth algorithm are applicability to dry snow only with a maximum retrievable snow depth of 0.50 m. This is because the 37-GHz channel does not see the ice surface beyond that depth so deeper snow does not further change the brightness temperature [*Kunzi et al.*, 1982]. Modeling studies have shown that the utilization of AMSR-E's lower frequency channels may circumvent this problem in the future [*Markus et al.*, 2006a]. For the Arctic, the algorithm is also limited to seasonal sea ice because of the similar radiometric signature of deep snow and multiyear ice. Importantly, changes in snow physical properties as well as the roughness of the underlying sea ice can affect the retrieval [*Stroeve et al.*, 2006]. Previous validation efforts in the Arctic

[1]Australian Antarctic Division and Cooperative Research Centre for Antarctic Climate and Ecosystems, University of Tasmania, Hobart, Tasmania, Australia.
[2]NASA Goddard Space Flight Center, Greenbelt, Maryland, USA.
[3]CliC International Project Office, Norwegian Polar Institute, Tromsø, Norway.

Copyright 2008 by the American Geophysical Union.
0148-0227/08/2007JC004181$09.00

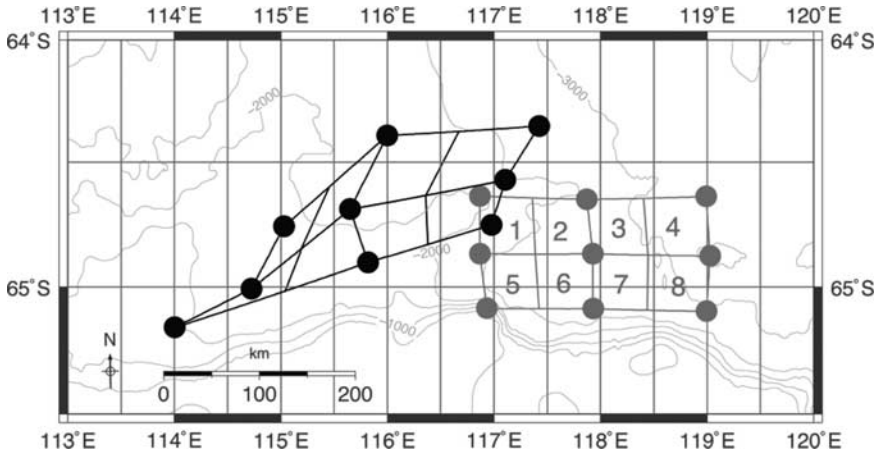

Figure 1. ARISE study region, showing the original deployment locations (grey circles) of nine drifting buoys on 26 September 2003, and their subsequent locations (black circles) on 16 October 2003. The eight Lagrangian grid cells referred to in the text are shown. This is a corrected version of Figure 1 of *Massom et al.* [2006].

using airborne passive microwave data [*Markus et al.*, 2006b] have shown that the order of magnitude in microwave snow depth retrievals over different sea ice regimes is well reproduced, but correlations with in situ snow depth are lower for areas of rough sea ice compared to smooth sea ice [*Maslanik et al.*, 2006]. Mean observed snow depths ranged from 8.1 cm for smooth ice to 19.1 cm for rough ice, which compares to microwave retrievals of 10.3 and 25.7 cm, respectively. Overall, snow depth was well correlated with sea ice roughness [*Sturm et al.*, 2006]. Modeling studies have shown that the lower correlation between in situ and microwave-derived snow depth for rough ice is likely caused by a change in effective sea ice surface emissivity with roughness [*Powell et al.*, 2006; *Stroeve et al.*, 2006]. Nevertheless, these comparisons were performed with airborne microwave measurements with a spatial resolution of only about 30 m, and over Arctic sea ice which has considerably different properties to Antarctic sea ice, which is the subject of this paper.

[5] Validation of the actual AMSR-E snow depth retrievals using field data is nontrivial because of the different spatial scales between satellite and in situ measurements. It is therefore necessary to ''merge'' the field observations to provide estimates of snow thickness at spatial scales comparable to the satellite sensor, since there is no efficient technique to accurately measure snow thickness over scales of hundreds of meters to kilometers. A key factor is to do this in as short a period as possible to avoid the effects of temporal variability. In this paper we present a methodology that combines in situ measurements of snow and ice thickness, airborne photography and drifting buoy data, to characterize an area of Antarctic sea ice, and to then compare our results with satellite-derived data over the same region. We focus particularly on the validation of AMSR-E snow depths and the effect of different ice and snow conditions on satellite retrievals. We also present a hemispheric comparison of the AMSR-E data with QuikSCAT radar scatterometer data and ship-based snow thicknesses from the ASPeCt (Antarctic Sea Ice Processes and Climate) database. Additionally, we show some coincident EOS Terra Moderate-resolution Imaging Spectroradiometer (MODIS) data for a qualitative comparison.

2. Data

[6] The ''Antarctic Remote Ice Sensing Experiment'' (ARISE) took place in September-October 2003 aboard the icebreaker RSV *Aurora Australis*, in the region 64°S–65.5°S, 112°E–119°E. An array of nine Lagrangian drifting buoys was deployed to define the study region and to monitor sea ice drift and deformation over a 3-week period. Figure 1 shows the deployment locations of the buoys on 26 September and their location 20 days later on 16 October. The original deployment locations defined a 4×2 grid with each cell having an initial size of approximately 25×25 km, representative of passive microwave scales. Throughout the experiment, ice stations were conducted from the ship in all but two of the eight Lagrangian grid cells. Helicopters were also used to gain access to floes remote from the ship and to conduct aerial photography over the buoy array. The study region was comprised entirely of first-year sea ice, much of which was deformed. The mean ice drift speed during the experiment was 11.1 km d^{-1}. *Massom et al.* [2006] provide a comprehensive overview of the data acquired during the voyage.

[7] Information on the snow cover thickness and characteristics was acquired using two quite different sampling strategies. First, long ice stations were conducted at 13 different locations throughout the study region, each separated by tens of kilometers. At these ice stations detailed in situ measurements were made of ice and snow properties along 100- to 500-m-long transects. The sea ice and snow thickness measurements were made at 1 or 2 m spacing along the transect, while ice cores and detailed snow pit measurements were made at 50- or 100-m intervals. The ice cores were analyzed for crystal structure, salinity and $\delta^{18}O$, while the snow pit information recorded grain size, density, salinity and wetness. The second method of data collection involved accessing ice floes by helicopter. These stations were at random locations within the buoy array that were

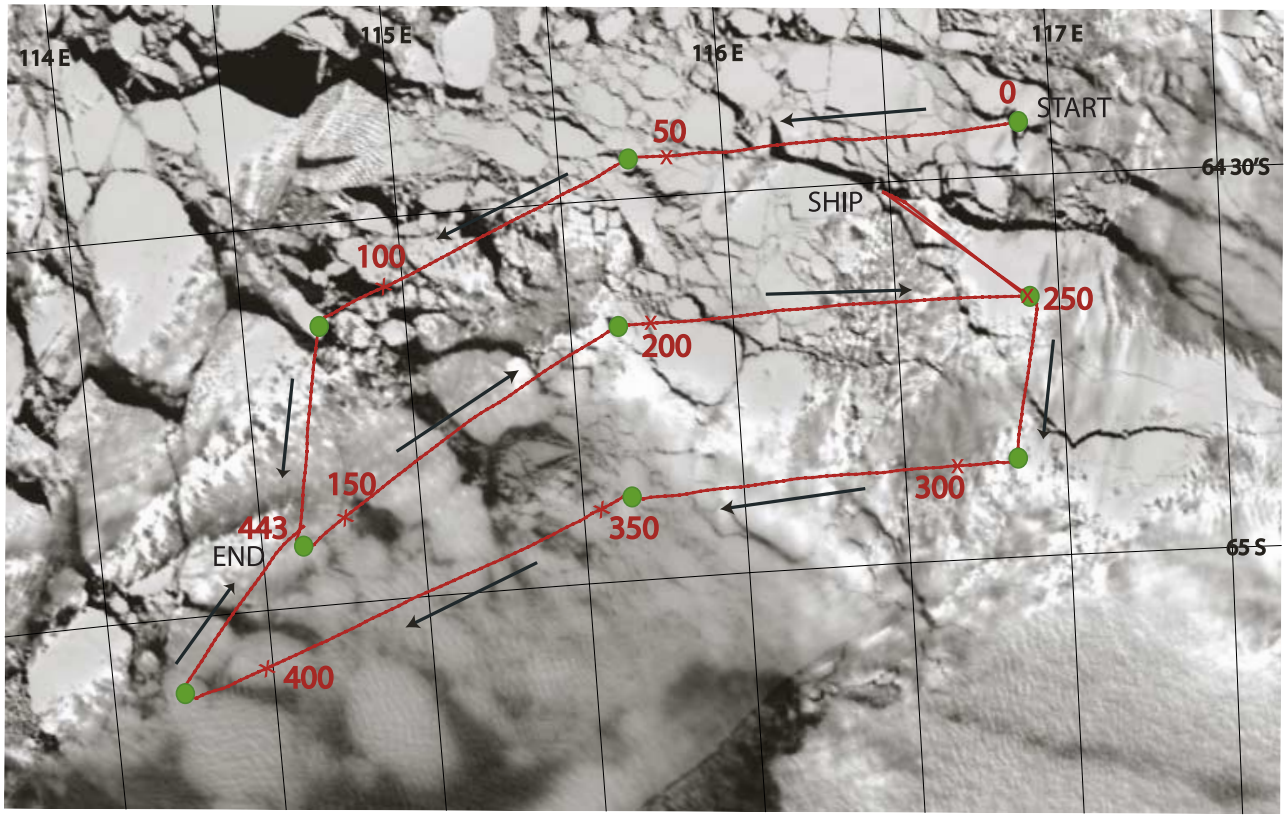

Figure 2. MODIS image over the study region at 0110 GMT on 8 October 2003. The locations of the nine drifting buoys are shown by green dots. The location of the ship and the start and end of the aerial photography flight line are shown. The red line shows the route of the helicopter over the buoy array with the direction of travel shown by black arrows. The numbers shown in red correspond to the approximate location of the sequential images taken during the flight, marked with a red cross. These numbers correspond to the *x* axis on Figure 10. A total of 443 aerial photos were taken between 2330 GMT on 7 October and 0400 GMT on 8 October. The dog leg in the flight track between image 250 and the ship is a refueling stop on which no photos were taken.

selected using a random number generator to generate latitude and longitude. The objective of these "mini" stations was to collect snow thickness information from as many sites as possible within the buoy array and consequently the time on station was limited to 15 min. Over a 15-day period between 29 September and 13 October we accessed 181 ice floes by helicopter and at each location we made two distinct sets of snow thickness measurements over the level and deformed parts of each floe.

[8] Digital aerial photographs were collected on six flights over the buoy array and provide an important layer of spatial data that bridges the gap between the coarse resolution satellite data and the in situ measurements. The photographs were collected using a Nikon D1x digital camera mounted looking directly downward through a hole in the floor of a helicopter. A handheld GPS was connected to the camera so that the latitude and longitude of each image was recorded as part of the image header file. The flights were conducted at an altitude of 5000 feet using a 28-mm lens, yielding an image resolution of approximately 0.40 m. Each image covers approximately 1200 × 800 m on the ground, with images taken consecutively (with about 5% overlap) to ensure total coverage along the flight track. In this paper we focus on Flight 4 which took place on 8 October, the only date on which the weather was clear enough to allow complete aerial photo coverage over the entire buoy array. The flight path over the nine drifting buoys is shown in Figure 2 overlaid on an EOS MODIS image from the same day. From each aerial photograph it is possible to determine the relative fractions of open water, thin snow-free ice, level ice with a relatively uniform snow cover and thicker deformed ice with a variable thickness snow cover, as described in detail below. The average snow thickness for each image was then calculated by combining this information with the in situ snow thickness measurements.

[9] During the voyage, single swath AMSR-E Level 2A brightness temperatures for our area of interest were collected by the U.S. National Snow and Ice Data Center (NSIDC) and emailed to the ship in near real time. The Level 2A data contain calibrated and geo-located brightness temperatures of each orbit to ensure the highest possible spatial and temporal accuracy, and these are used here for comparison with the in situ and aerial photography data. Since the cruise, improvements in AMSR-E calibration and geolocation warranted the use of the latest AMSR-E Level 2A brightness temperatures available at NSIDC (Version V08). The geo-location error of the AMSR-E data

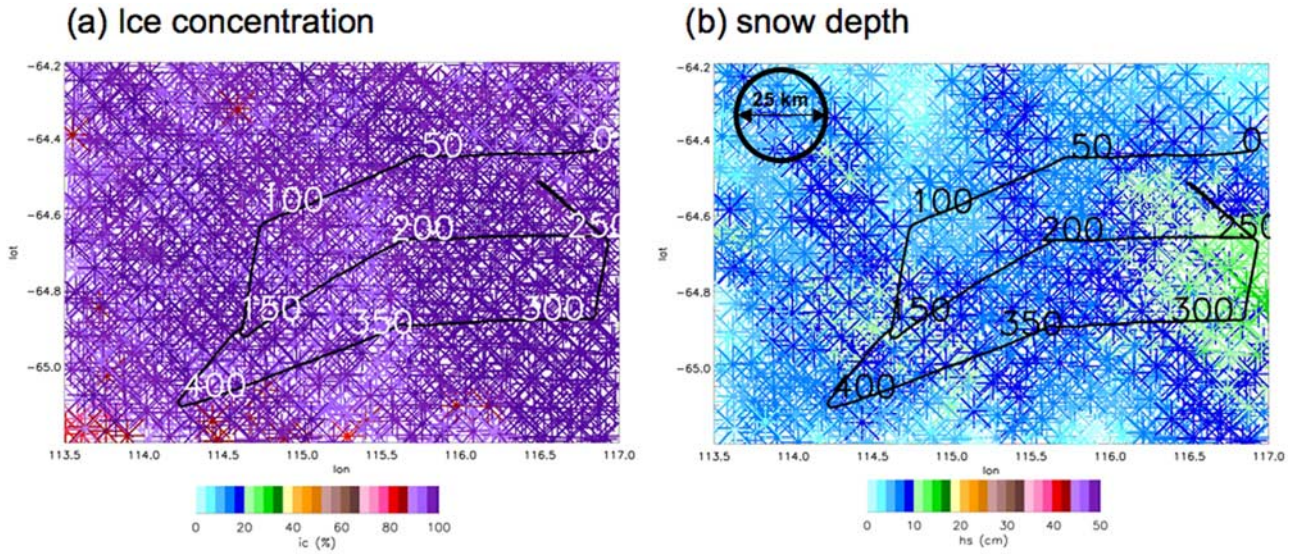

Figure 3. AMSR-E data showing (a) sea ice concentration and (b) snow depth for 7 October 2003. The black line shows ground track of Flight 4 and the numbers represent the approximate location of the sequential aerial photograph numbers along the track.

is about 1 km. Figure 3 shows the AMSR-E derived parameters of the study region with the ground track of Flight 4 shown in black. The density of points depends on the number of orbits that covered the area for a given day. Potential mismatches of the individual orbits have not been corrected owing to the relatively low drift speed of the ice. The images show that there is good spatial coherency in the data. The sea ice concentration shown in Figure 3a is generally close to 100%, while the snow depth is relatively uniform, increasing only slightly from west to east as shown in Figure 3b.

3. Data Analysis

3.1. In Situ Data

[10] Figure 4 shows snow pit data (Figure 4a) and thickness transect data (Figure 4b) collected at Station 2 on 28 September. At this site both the ice and snow thickness were highly variable, and the snow pit data reflect similar variability in snow properties. At snow pits A and B for example, the surface snow is soft 0.2- to 0.5-mm grains while pit C has a wind-packed crust. Different conditions are also found at the base of the snow layer at different sites: pit A having damp snow at its base, compared with dry snow at pit B and refrozen slush at pit C. This degree of local variability is consistent with the findings of many other papers, as summarized in the review by *Massom et al.* [2001], and poses a significant challenge for validation studies of remotely sensed data. Despite this, *Sturm et al.* [1998] note that at a regional level, fairly predictable stratigraphic and textural snow sequences develop each year because of the regular sequence of warm storms and cold periods that affect the evolution of snow properties (i.e., metamorphism). Our transect measurements also revealed that regions of thinner, level snow cover are typically associated with undeformed ice, compared with a thicker, more variable snow cover over deformed ice. Figure 5 shows ice and snow thickness data along a 500-m transect at Ice Station 4 on 2 October. This transect clearly shows a significant increase in snow cover thickness that coincides with the deformed parts of the floe; in other words the snow surface roughness appears to be largely determined by the roughness of the underlying ice. This is also consistent with the findings of *Sturm et al.* [1998] who reported that almost any ice surface feature >0.2 m produces corresponding features at the snow surface. While features such as barchan dunes can lead to significant snow thickness variability on smooth Antarctic sea ice on horizontal scales of 1–10 m [*Massom et al.*, 2006], these features were not frequently observed in our study region.

[11] Figure 6 shows the surface conditions encountered at one of the helicopter "mini" stations. This photograph is quite representative of conditions throughout the study region, showing distinct areas of rough and smooth snow cover. The regions of level ice are frequently interrupted by sea-ice ridge heights 1–2 m above the level ice surface, comprising blocks usually in the range 0.2–0.4 m thick but with no preferred orientation. Two sets of snow thickness measurements were made at each mini station, including up to 20 measurements over the level snow and a similar number over the rough snow. The ice/snow interface temperatures were also recorded, but not reported here. A total of 4856 measurements were made; 2947 of these were over the rough snow cover and 1909 over smooth snow cover. The mean thickness values represent a large-scale mean over the buoy array that smoothes the effects of precipitation and/or aeolian redistribution of snow during the experiment. The average thickness of the snow cover over rough ice was 0.36±0.22 m compared with 0.17±0.16 m over smooth ice.

3.2. Aerial Photography

[12] In order to classify the aerial photographs according to ice and snow cover type, a number of steps were taken. First, a simple thresholding technique was used to differentiate open water, thin snow-free ice and snow covered ice. These were determined by creating a binary image using a variable grey-scale threshold with an interactive slider tool.

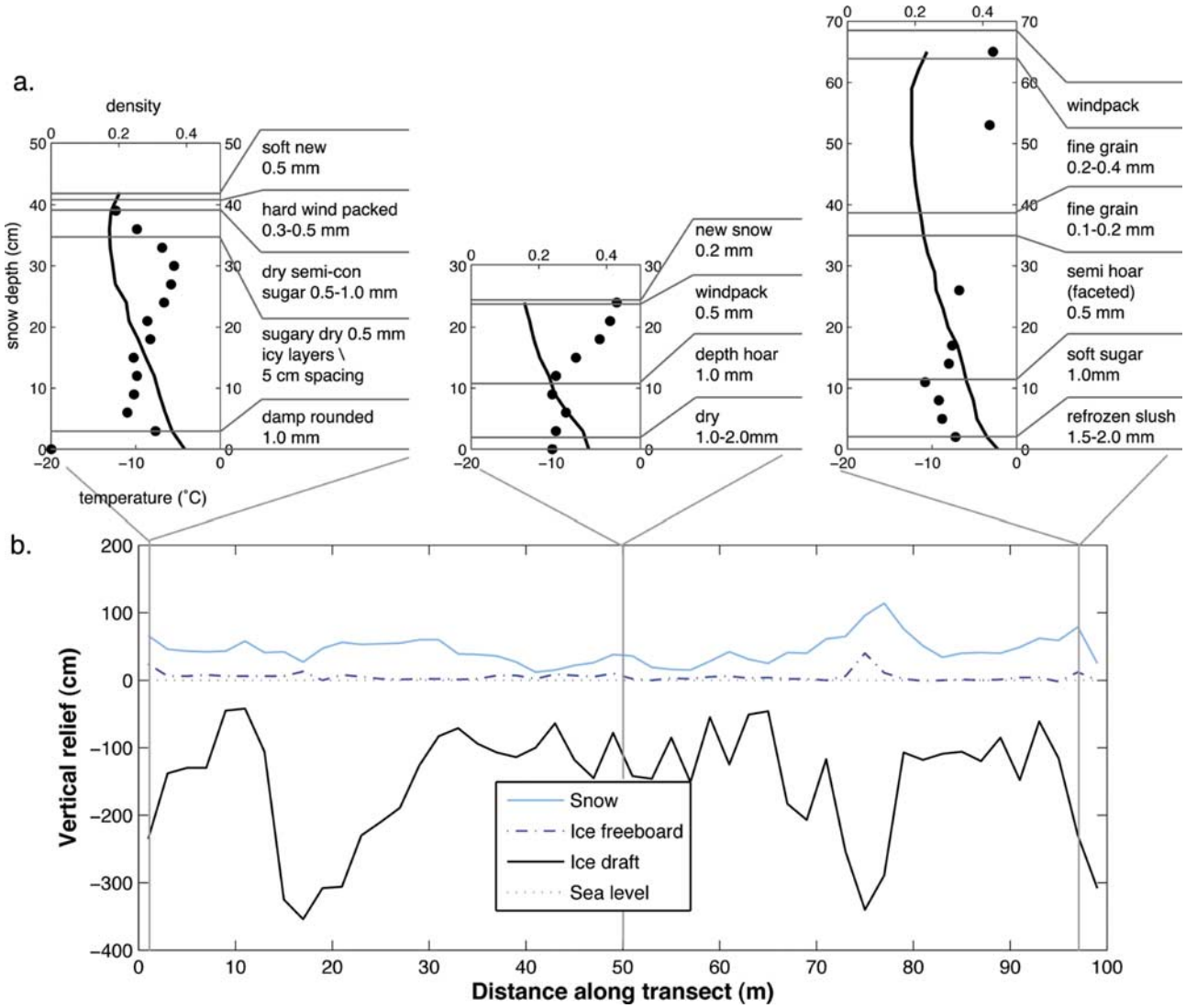

Figure 4. (a) Snow structure, temperature and density data for three snow pits at 0, 50, and 98 m along (b) the ice thickness transect. These data were collected at Ice Station 2 on 29 September at 64°48'S, 117°30'E.

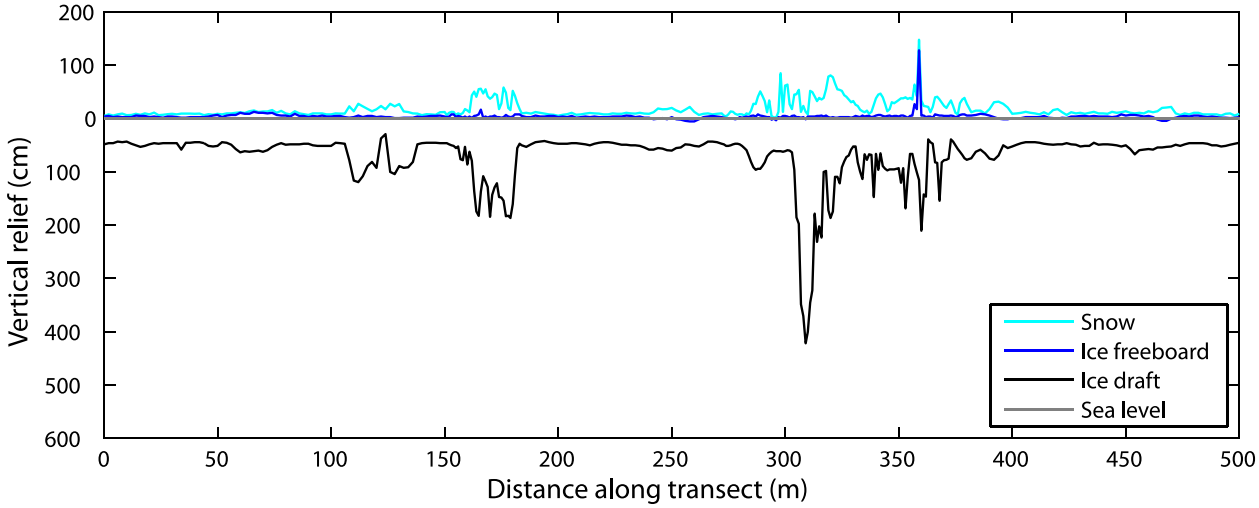

Figure 5. Ice, freeboard, and snow thickness data along a 500-m transect at Ice Station 4 on 1 October at 64°37'S, 117°46'E.

Figure 6. Photograph of a helicopter at a "mini" station. The smooth and rough surface conditions can clearly be seen in the image.

By varying the threshold up and down it is possible to identify the percentage of each surface type making up the image. Automated first guesses were made to speed up the processing time, but this needed to be checked manually to account for changes in exposure caused by changes in surface brightness.

[13] An additional procedure was developed to separate different snow surface characteristics, in particular areas of rough and smooth snow. It was evident from the images that these two distinct classifications were visible, but could not be separated using a simple thresholding technique. Instead we performed a texture-based analysis using a local binary pattern (LBP) operator [*Lucieer and Stein*, 2005; *Ojala et al.*, 2002; *Ojala and Pietikäinen*, 1999] to separate areas of level and rough snow cover in the images. An LBP operator for a given pixel is defined by the number of pixels with grey levels greater or less than the pixel of interest within a defined neighborhood set. For example, the LBP for a 3×3 area of nine pixels with one centre pixel and eight neighbors, is derived by thresholding the neighborhood using the grey value of the centre pixel. The LBP is represented as a set of zeros (for neighbors below the threshold) and ones (for neighbors above), and gives a grey-scale invariant measure of local texture. If three neighbors have grey values higher than the center pixel and five lower, the LBP operator assigned to the center pixel is 3. This tells us about the uniformity of a neighborhood with respect to the centre pixel, but not between the pixels that make up the neighborhood. To determine the latter we consider the number of times the sign of the difference between each pixel and the centre pixel changes. Going around the neighborhood (n) from n1 …. nN (for N neighbors), the uniformity operator is incremented by 1 each time there is a sign change. Of course, both operators are scale-dependent and therefore the width of the defined neighborhood will determine the size of texture elements that are identified.

[14] In addition to the LBP operator and uniformity operator, each pixel is also assigned a variance value for its neighbor set (VARc) and a contrast value (mean grey level) for its neighbor set. VARc is calculated as the variance of grey level contrast among the entire set, while the mean grey level is derived from the 3×3 neighborhood set around the centre pixel. Overall, four images are derived in the process, as shown in Figure 7: variance (Figure 7a), LBP (Figure 7b), uniformity (Figure 7c) and mean grey level (Figure 7d). These images form a texture, variance and contrast model which drives the subsequent image analysis procedure.

[15] LBP/VARc cooccurrence 2D histograms are generated by quantizing the image variance into S + 1 bins, where *S* is the total number of neighbors considered and each bin contains an equal number of data points. A cooccurrence matrix is then constructed using the derived LBP, which is a discrete variable having 0→S-1 as possible values. We then made a function that generates appropriate variance bin cut values using the overall image variance as a model. Using these values to bin variance we then generated a 2D histogram of variance and the chosen texture operator.

[16] The LBP, uniformity and VARc images were used as criteria for splitting the image into blocks of homogeneous texture. First, the whole image was split into square subblocks of user-defined size. Each block was recursively processed by an algorithm which split the block into four subblocks, compared the joint distribution (2D histogram) of a texture operator and VARc in each subblock, then determines whether to split the subblocks further on the basis of on a user-defined histogram similarity threshold. Histograms were compared using a nonparametric two-way test known as the log-least-likelihood, or G statistic. This test computes various bin-wise and whole-of-histogram sums, comparing the values in each bin of each histogram, and returning a numerical measure of relative histogram similarity. Low G values indicate similar histograms, while high G values indicate dissimilar histograms. In order to decide whether to split a block, a ratio of the minimum and maximum G statistics of its subblocks was obtained and compared to the preset splitting threshold. Recursive splitting is continued until the

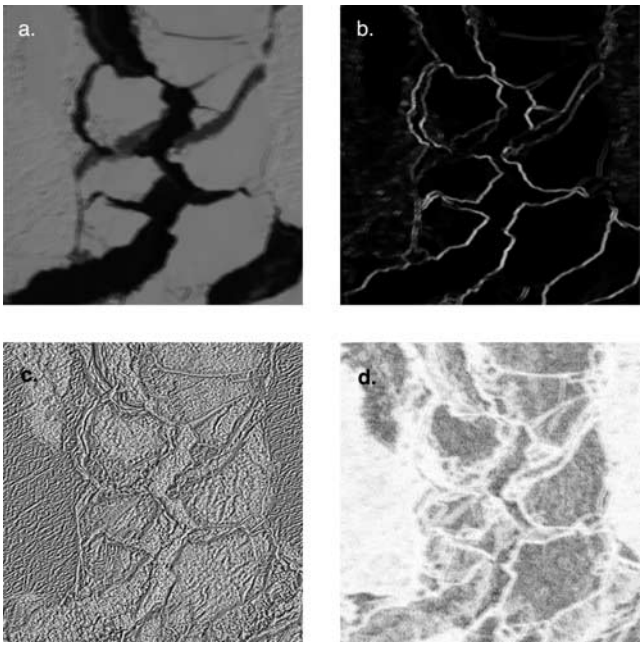

Figure 7. Images derived during the image analysis procedure, as described in the text.

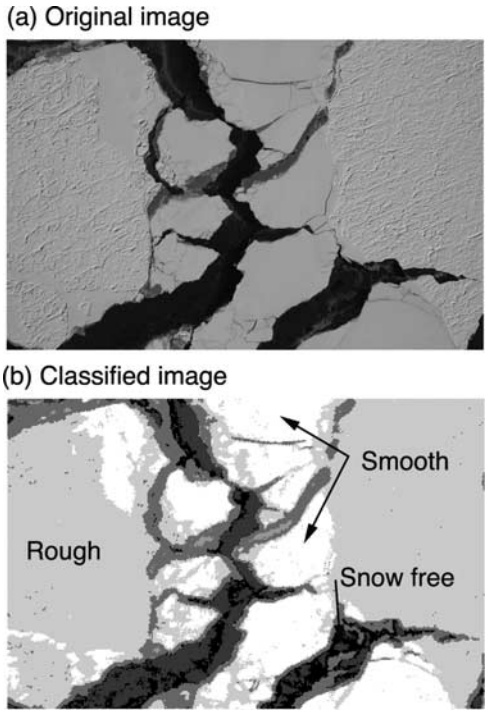

Figure 8. (a) An aerial photograph of Antarctic sea ice, showing different surface characteristics and ice types. (b) Classified image showing different surface classes determined by textural image analysis described in the text.

histograms for four subblocks are not sufficiently different, or a preset minimum block size is reached.

[17] "Smooth" and "rough" surfaces were experimentally determined using several test images from the set used in this paper, and rely on the scale of features, and the general texture characteristics of image subblocks. The size of features was examined to check whether "roughness" was based on small contrast differences or actual features on the snow. We tuned the software to see "rough" or "smooth" surfaces in the same way a person looking at the surface would. In the block-splitting algorithm, a texture value was applied to each block according to its modal "roughness". A "roughness" threshold was then applied, chosen to give the best match to areas of "rough" and "smooth" snow covered ice in the aerial photograph being analyzed. The scale and roughness threshold were the same for most of the images analyzed, on the basis of experimenting with subsets of aerial photographs from the voyage.

[18] Figure 8 shows the result of this image processing technique. Figure 8a is the original image, approximately 1200 × 800 m in size and clearly shows areas of open water, snow-free ice, level snow covered ice and rough snow covered ice. Figure 8b is the processed image, which returns the percent cover of each of these surface types. Results from an automated classification process were compared with the sliding scale technique described above, and any results which differed by more than 20% in concentration of any ice type were manually reassessed. A small number (26) of a total of 443 images were misclassified and corrected manually. These differences occurred either when there was a very bright surface (e.g., sun glint) that was misclassified as snow, or when there were irregular shadows over an image caused by high cloud. Future development of the algorithm will attempt to overcome these problems.

4. Results and Discussion

4.1. Comparison of Merged Field Measurements and Satellite-derived Snow Thicknesses

[19] The relative percentages of the four surface types identified in the aerial photography analysis are shown in Figure 9. These are (1) rough snow surface, (2) smooth snow surface, (3) thin (snow-free) ice, and (4) open water. As described above we use the surface roughness as a proxy for snow depth and have assigned mean snow thicknesses of 0.36 m for snow over rough ice and 0.17 m for snow over smooth ice, on the basis of the mini station data. As shown in Figure 9 most images contain > 80% rough ice/snow. Figure 10 compares the field measurements with the AMSR-E data for Flight 4. The x axes in Figure 10 represent the image numbers (from 1 to 443) that are shown in red on Figure 2. In the polar regions, there is normally more than one orbit per day covering any given region. For a comparison with in situ data this gives us the option between best spatial or best temporal coincidence. The best spatial agreement is achieved through the use of the pixel closest to the in situ measurement, independent of the orbit. Additionally, extended in situ measurements often take several hours to acquire whereas satellite observations over a small region take only a few seconds. For these reasons, results using the best spatial agreement as well as the early and late orbits each day are used. This approach also helps to demonstrate diurnal variability. Given that the mean ice drift is subpixel scale we have not corrected for ice drift when choosing the best spatial agreement between aircraft and satellite observations.

[20] To facilitate the comparison we apply a 25-km running mean to the aerial photography data. The ice concentration data in Figure 10 (top) show good spatial agreement between the two data sets. The differences between the early and late orbit data illustrate the rapidity

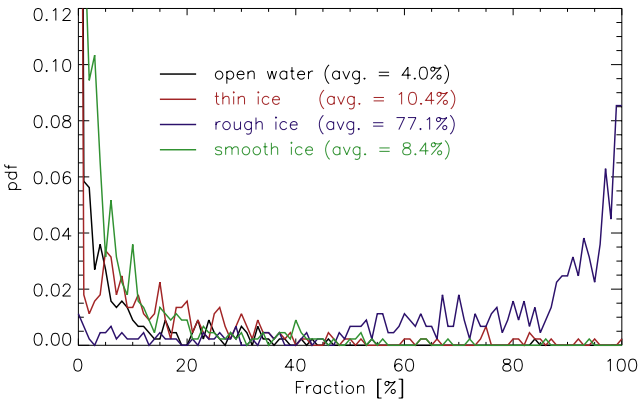

Figure 9. Probability density functions (pdf) of open water, thin ice, rough ice, and smooth ice from the aerial photography. The pdf is plotted versus the corresponding fraction for each ice type. The actual maximas at 0% are 0.60 for open water, 0.50 for thin ice, and 0.18 for smooth ice. To assist with interpretation of this plot, the point x = 90, y = 0.025 for the blue line, indicates that 2.5% of images have exactly 90% rough ice.

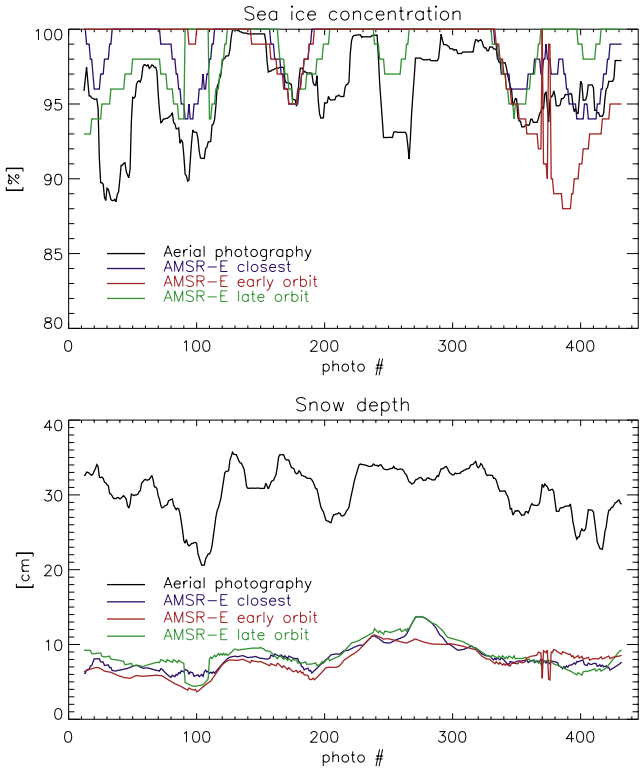

Figure 10. (top) In situ ice concentration and corresponding AMSR-E ice concentration, plotted. (bottom) AMSR-E snow depths. All data are plotted as a smooth 25-photo (~25 km) running mean. The AMSR-E pixels closest to the flight line (but independent of orbit) are blue. The red and green lines show the AMSR-E ice concentration and snow depth from the earliest and latest orbits on 8 October.

of ice concentration changes as a result of sea ice dynamics or the freezeup of leads. The snow thickness data shown in Figure 10 (bottom) however, are not in good agreement. While some broad spatial agreement is clear, the AMSR-E data are significantly lower and have a lower dynamic range. The in situ snow depth ranges from 0.2 to 0.35 m while the coincident AMSR-E snow depth ranges between 0.04 and 0.14 m. The correlation between in situ snow and AMSR-E snow depth is nevertheless 0.52 (when using individual orbits the correlation coefficients vary between 0.48 and 0.66), indicating a reasonable agreement in spatial variability (Table 1).

[21] Given that the AMSR-E sea ice concentration is an input parameter into the snow depth algorithm, its sensitivity to the results is also investigated. *Markus and Cavalieri* [1998] estimated a sensitivity of approximately 1 cm per 1% sea ice concentration error. Here we are using (1) a constant ice concentration of 100% and (2) the aerial photography ice concentration, which do not change the correlations significantly (Table 1, bottom two rows). However, the correlation coefficients between the AMSR-E brightness temperatures themselves show unexpected variations as a function of frequency. As mentioned in section 1, the effect of snow depth is expected to be most strongly reflected at 37 GHz. The brightness temperature at this frequency is expected to decrease with increasing snow depth, resulting in a greater difference between 19- and 37-GHz TBs; that is, the 37-GHz TBs are expected to have a strong negative correlation with snow depth. In this data set, the 37-GHz TBs correlation coefficients are positive and are the smallest compared to the other frequencies, while the lower frequencies have a greater positive correlation with snow depth. For this reason the difference between 19- and 37-Ghz TBs is again correlated with snow depth. The nature of our approach (i.e., assigning constant snow depths for rough and smooth ice, and zero snow depth for thin ice) results in a strong correlation between the fraction of rough ice and in situ snow depth. The positive correlation coefficients and the increase in value with decreasing frequency suggest that the ice roughness is dominating the signal.

[22] The potential for using lower frequency channels to account for sea ice roughness has been shown for Arctic conditions by *Stroeve et al.* [2006] who found that the effective incidence angle decreases with increasing small-scale ice thickness variability. The emissivity of sea ice generally decreases with increasing incidence angle [e.g., *Grenfell et al.*, 1994]. The nominal incidence angle for AMSR is 55° but for rough sea ice the effective incidence angle can be as low as 35° [*Stroeve et al.*, 2006], which would explain the higher brightness temperatures for areas with large fractions of rough ice. This indicates the importance of developing dynamic algorithm coefficients that account for sea ice roughness. As described above the AMSR-E snow depth algorithm saturates at about 0.5 m. To investigate its potential effect on this comparison we set all in situ snow depth measurements greater than 0.5 m to 0.5 m. This resulted in an insignificant average reduction in the in situ snow depth of 0.04 m.

4.2. Lagrangian Comparison

[23] In this section we compare the in situ data collected between 29 September and 13 October with the level 3 AMSR-E snow depth product over the same time frame. The beacon positions were utilized to extract the corresponding AMSR-E pixel for each day and for all eight grid cells.

[24] The mini station snow thickness data were distributed across six of the eight Lagrangian grid cells that we now

Table 1. Correlation Coefficients Between AMSR-E Data and In Situ (Aerial Photography and Mini Station) Data[a]

AMSR-E Parameter	Correlation with In Situ Snow Depth (Early, Late Orbit)
TB_{6V}	0.55
TB_{6H}	0.54
TB_{10V}	0.64
TB_{10H}	0.57
TB_{18V}	0.60
TB_{18H}	0.63
TB_{37V}	0.31
TB_{37H}	0.49
TB_{89V}	−0.6
TB_{89H}	−0.49
Snow depth	0.52 (0.48, 0.66)
Snow depth (IC = 100%)	0.60 (0.58, 0.63)
Snow depth (IC from in situ)	0.60 (0.58, 0.63)

[a] The last three rows show the correlation between AMSR-E snow depth and in situ snow depth. Since the snow depth retrieval is somewhat dependent on the sea ice concentration retrieval, we also show results using (1) a constant ice concentration of 100%, and (2) the ice concentration derived from the in situ data. IC stands for ice concentration.

Table 2. Statistics for the Eight grid Cells as Indicated in Figure 1[a]

Grid Cell	Area on 29 September, km^2	Area on 13 October, km^2	In Situ Snow Depth (Constant), cm	In Situ Snow Depth (Variable), cm	AMSR-E Snow Depth, cm	QuikSCAT Backscatter, dB	Correlation AMSR-E Snow Depth and QuikSCAT Backscatter
1	637	242	28.7	18.7	13.2	−16.5	0.80
2	639	345	30.0		13.1	−16.9	0.64
3	780	1225	27.1	30.0	12.6	−17.0	0.32
4	787	843	32.0	23.8	13.3	−17.1	0.34
5	639	17	27.1		12.0	−17.0	0.57
6	629	653	29.5	24.4	13.1	−17.2	0.79
7	702	762	28.9	29.6	12.7	−17.2	0.49
8	781	649	32.6	36.9	12.8	−17.1	−0.29

[a]The area at the beginning and at the end of the observation period is determined by the drifting buoy positions. The values for the "constant" in situ snow depth are calculated by averaging the in situ measurements for rough and smooth surfaces, respectively, independent of box number and by utilizing the fractions of thin, smooth, and rough surfaces from the aerial photography. For the "variable" in situ snow depths, only measurements for along the edge of the respective grid cells were considered in calculating the mean values. No in situ measurements were taken in boxes 2 and 5. The AMSR-E snow depths and the QuickSCAT backscatter values are averages over the 15-day period following the grid cells. The correlation coefficients are determined using daily data.

use to calculate mean snow thicknesses for each of those cells (excluding cells 2 and 5 which have no data). Using the aerial photography bordering each grid cell to determine the fractions of each of the four surface types (rough and smooth ice, thin ice and open water), we have calculated the mean snow thickness. These are shown in column 4 of Table 2. We also use the overall mean snow thickness values (0.36 m for rough and 0.17 m for smooth ice) from the previous section to calculate and alternative mean for each grid cell that is presented in column 5 of Table 2. We have done this because of concern that the number of observations in each cell is correlated with snow depth [*Massom et al.*, 2006, Figure 2]. These two data sets are plotted in Figure 11, which shows a better correlation (0.63) between the AMSR-E snow depths and the overall mean in situ snow thickness value, compared to the values for individual grid cells. The reason for this is that there are not enough observations in each grid cell to give an accurate mean thickness for each. The actual AMSR-E snow depth values are about a factor of 2.3 too low, which poses the question as to why *Markus and Cavalieri* [1998] found such good agreement with in situ data, reporting a bias of only 3.5 cm. This is perhaps related to the in situ data used to determine the algorithm coefficients, which were from field data over predominantly level ice that probably do not represent the true average snow depth. This is discussed in more detail below.

[25] As mentioned above, previous studies have also highlighted problems in the snow depth retrieval over rough sea ice. We therefore compare our results with backscatter values from QuikSCAT available from the Physical Oceanography DAAC at the Jet Propulsion Laboratory, Pasadena, California [*Long*, 2000]. Figure 12 shows a map of vertical polarization backscatter for 8 October 2003. Backscatter values for sea ice range between −20 and −10 dB and generally increase (become less negative) with increasing roughness. Values of −20 dB correspond to smooth ice and values of −10 dB to rough ice. In the East Antarctic region, the backscatter values are between −15 and −16 dB for the outer pack and between −17 and −18 dB closer to the coast, where our measurements were taken (Figure 13). The average backscatter is rather constant over the eight grid cells (Table 2), with a value of about −17 dB being indicative of relatively smooth first-year ice [*Long and Drinkwater*, 1999]. A snapshot comparison between AMSR-E snow depths and QuikSCAT backscatter does not properly separate true snow depth variability from erroneous retrievals caused by changing surface roughness. As evident in Figure 12, some regions, like in the western Weddell Sea, show clear spatial correlation between snow depth and backscatter while others do not. Factors explaining areas of correlation include the fact that deeper snow is often observed in areas of rough ice [e.g., *Massom et al.,* 1998; *Sturm et al.*, 2006] (also this field experiment) and that an increase in snow depth in expected to increase the backscatter [e.g., *Onstott*, 1992], especially over smooth ice. A lack of spatial correlation could simply be indicative of a lack of connection between snow depth and roughness but could also be caused by erroneous snow depth retrievals as a result of changes in snow and/or ice radiometric properties.

[26] The eight Lagrangian grid cells provide an ideal data set for investigating the temporal correspondence between AMSR-E snow depth retrievals and radar backscatter caused by changes in roughness. The correlation coefficients are significantly positive for all but grid cell 8 (Table 2, right column, and Figure 14), which is the only grid cell to show an increase in snow depth. The backscatter data

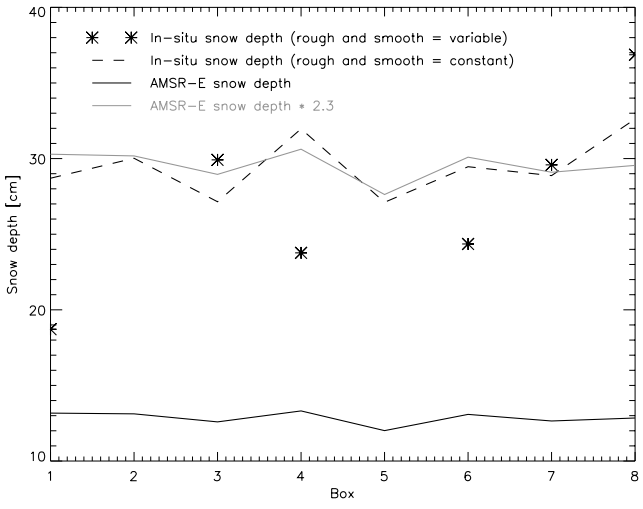

Figure 11. In situ and AMSR-E snow depths for the eight Lagrangian grid cells. The data are taken from Table 2.

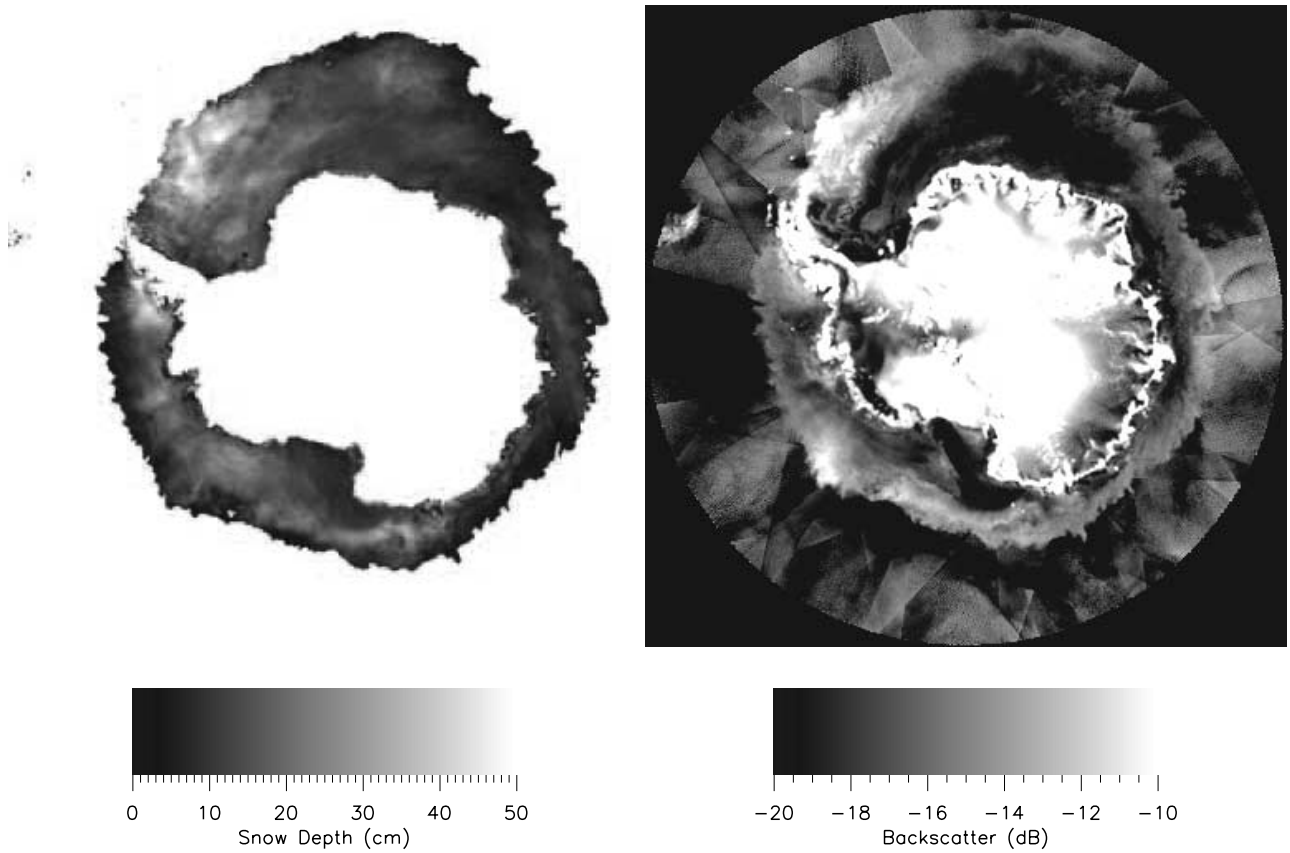

Figure 12. (left) AMSR-E snow depth and (right) vertical polarization QuikSCAT backscatter for 8 October 2003.

suggests a trend toward smoother ice (or more thin ice), however this is inconsistent with the observed convergence of some of the Lagrangian grid cells. The highest correlations are observed for the grid cells where the area is decreasing (for example, grid cell 1), suggesting that other processes are affecting the radar backscatter. Figure 14 shows both the QuikSCAT backscatter and AMSR-E snow depth have negative trends, with significant decreases (especially in radar backscatter) from 4 to 5 October. This is coincident with a major storm responsible for strong winds of 45 knots and air temperatures rising to near the melting point. A series of repeat in situ measurements at Ice Station 4 late on 5 October showed significant new flooding at the ice/snow interface that was not present on 1 October. If this was widespread over the entire study region it is a possible explanation for the observed decrease in backscatter, as the flooding would effectively have smoothed the ice surface and significantly altered the microwave emissivity of the ice. This is also consistent with the observed reduction in snow depth. Ice core data and thickness measurements from this, and other, studies [*Lange et al.*, 1990; *Jeffries and Weeks*, 1992; *Worby et al.*, 1998] have shown that flooding and snow ice formation is ubiquitous throughout the sea ice zone. However, this limited data set is suggestive of the possibility that widespread flooding may occur in response to a single synoptic event, with far-reaching implications for satellite remote sensing retrievals. This is an important temporal process that should be the subject of further sea ice field studies.

4.3. Comparison of AMSR-E Snow Depth with Ship-based Observations

[27] Snow thickness data on Antarctic sea ice are also available from the Antarctic Sea Ice Process and Climate (ASPeCt) data archive, described in detail by *Worby et al.* [2008]. For the ARISE cruise in 2003, 178 individual ship-based observations were made within the study region (with a minimum distance criteria of 6 nautical miles between consecutive observations). The observations south of 64°S,

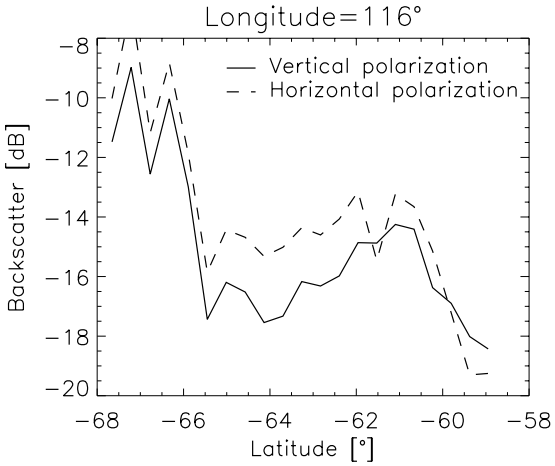

Figure 13. Latitudinal variability in QuikSCAT backscatter along 116°E.

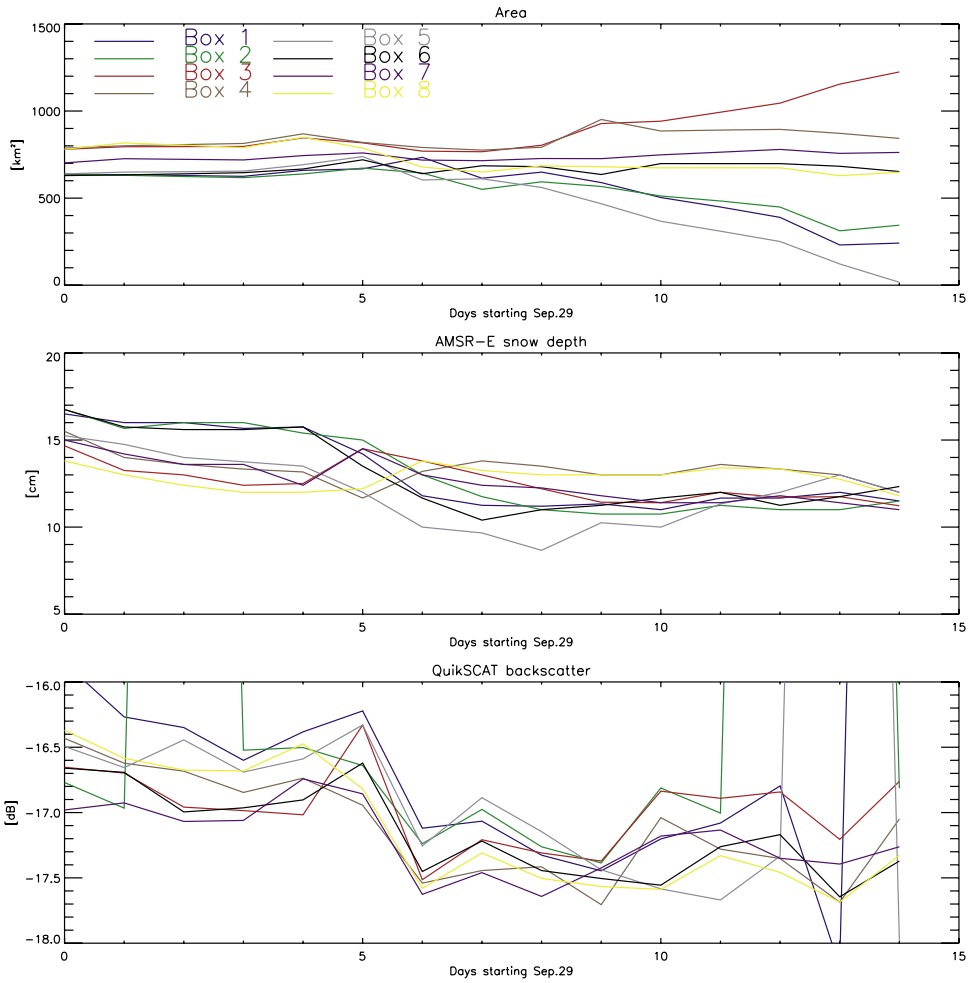

Figure 14. Area and corresponding AMSR-E snow depth and QuikSCAT backscatter for the eight Lagrangian grid cells. The increasing number of missing QuikSCAT data toward the end of the period is a result of the decreasing areas of grid cells 1, 2, and 5.

which exclude the ice in the marginal ice zone have a mean ice concentration of 90%, mean ice thickness (including ridged ice) of 0.85 m and mean snow thickness of 0.12 m. The ice and snow thicknesses are averaged over the total area including the open water. The snow cover reported in the ship observations is 0.05 m less than from the level in situ observations reported above, which have an average of 0.17 m. This most likely reflects the fact that thinner ice with thinner (or no) snow cover (such as nilas) is reported in the ship-based observations, but obviously not in the in situ measurements, given that it is too thin to walk, or land aircraft, on.

[28] In addition to the ship-based observations for this voyage, the ASPeCt archive also contains data from 80 other voyages to all regions of the Antarctic pack ice between 1980 and 2005 [*Worby et al.*, 2008]. Figure 15a shows the annual mean snow cover thickness from the AMSR-E data on a 100 km grid, while Figure 15b shows the mean annual snow thickness from the ASPeCt data. Clearly the spatial coverage of the ship observations is not as good as the satellite data; however there is broad agreement between the areas of thinner and thicker snow cover around the continent. The East Antarctic region shows excellent agreement between the two data sets, within a range of ±0.10 m. This region represents the best seasonal coverage of ship observations and a regime of mostly first-year ice that is thicker near the coast and thinner toward the ice edge. Similarly good agreement is observed in the Bellingshausen/Amundsen Seas, the tip of the Antarctic Peninsula and most of the Ross Sea. On the basis of comparisons with in situ measurements the accuracy of ship observations is ±0.2 m for typical snow cover thicknesses within the Antarctic pack. However, it is important to note that these are acknowledged as being representative only of the snow cover on level sea ice. The ASPeCt observation protocol specifies that the thickness of level ice and snow cover are recorded, together with estimates of surface ridging that are used to correct the level ice thickness for the mass of ice in ridges [*Worby et al.*, 2008]. However, a similar correction for snow cover thickness is not possible on the basis of the recorded data, so the reported snow thicknesses are representative only of the level portions of ice floes. It is therefore highly probable that the reason for the good agreement between the AMSR-E snow thicknesses and the ASPeCt snow thickness data, is that both sets of observations are more representative of snow cover over

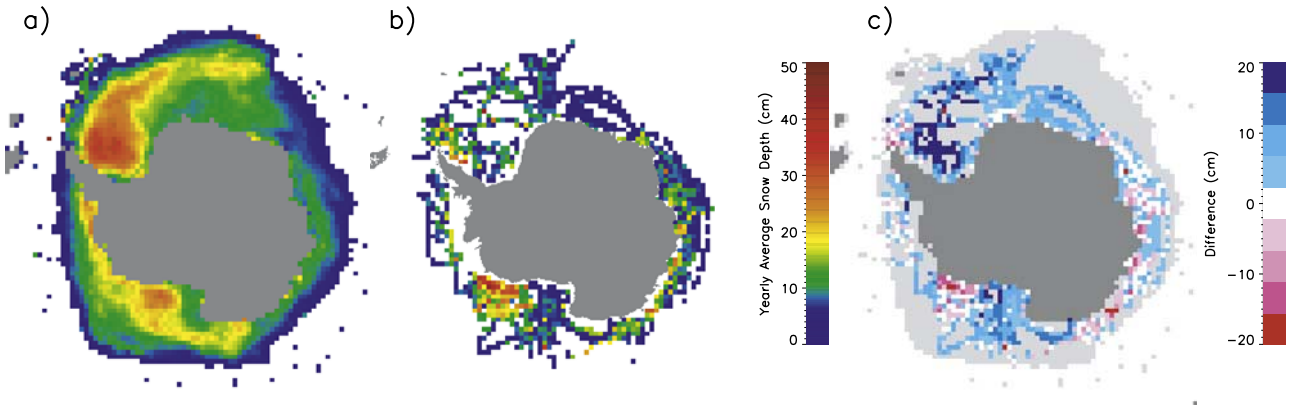

Figure 15. Mean annual snow thickness from (a) AMSR-E and (b) ship-based snow thickness observations in the ASPeCt data archive. (c) Difference between AMSR-E and ship-based observations of snow thickness (AMSR-E minus ASPeCt).

level ice. This also goes some way to explaining the good agreement between large-scale in situ and passive microwave derived snow depths reported by *Markus and Cavalieri* [1998] which also essentially measured the snow depth on level ice.

5. Conclusions

[29] Several important conclusions can be drawn from this Antarctic field experiment.

[30] 1. The AMSR-E-derived snow depths are significantly lower than the in situ snow depths measured over East Antarctic pack ice during Spring. This is different from previous comparisons in the Antarctic [*Markus and Cavalieri*, 1998] and the Arctic [*Maslanik et al.*, 2006], which we believe is related to a bias toward measurements of thinner snow in ship-based and in situ measurement programs.

[31] 2. As in the Arctic, sea ice roughness appears to be a major source of error in the retrieval of snow depth from satellite passive microwave data over Antarctic sea ice.

[32] 3. The Lagrangian analysis showed a decrease in snow depth and backscatter in a convergent sea ice field. The corresponding decrease in snow depth and backscatter is quite likely caused by widespread flooding which would effectively smooth the sea ice. The potential of flooding and the ice/snow interface as a major source of error in underestimating snow depth requires further investigation.

[33] 4. QuikSCAT (or other scatterometer) backscatter data have provided useful insights into processes that may be influencing the passive microwave signals. These data could therefore be used in future to adjust the AMSR-E snow depth algorithm coefficients.

[34] 5. The AMSR-E snow depth algorithm was compared with large-scale routine measurements of snow depth from the ASPeCt ice observations. Since snow depth measurements are observed only over the level portion of ice floes, it is now apparent that these data underestimate the true mean snow thickness because the thicker snow cover on deformed ice is not included [*Worby et al.*, 2008].

[35] 6. Future work must include field and aircraft observations over a broader range of surface types, in particular level ice surfaces, which could be found in regions of undeformed fast ice. Unfortunately, there was no opportunity during this experiment for observations over large expanses of uniformly level ice, hence the performance of the AMSR-E product over level ice could not be adequately assessed.

[36] 7. Good agreement was observed between the AMSR-E derived ice concentration and the in situ measurements and aerial photography, effectively eliminating this as a likely source of the observed error in the snow thickness algorithm.

[37] **Acknowledgments.** We wish to thank the captain and crew of RSV *Aurora Australis* for their support, together with the helicopter pilots and engineers aboard the ship. The Casey expeditioners are also acknowledged for their help with in situ measurements. Arko Lucieer is thanked for his assistance with the development of the image processing software and Jeff Miller of RSIS at NASA/GSFC is acknowledged for his help with the graphics. This work was carried out as part of Australian Antarctic Science Project 2298 and was supported by the Australian Government's Cooperative Research Centres Program through the Antarctic Climate and Ecosystems Cooperative Research Centre (ACE CRC). The work also forms part of NASA's AMSR-E Validation Program through NRA-OES-03. AMSR-E data were obtained from the NASA Earth Observing System Distributed Active Archive Center (DAAC) at the U.S. National Snow and Ice Data Center, University of Colorado, Boulder (http://www.nsidc.org). MODIS data were obtained from NASA's Distributed Active Archive Center. QuikScat data were obtained from NASA's Scatterometer Climate Record Pathfinder data set at Brigham Young University.

References

Chang, A. T. C., J. L. Foster, and D. K. Hall (1987), Nimbus-7 SMMR derived global snow cover parameters, *J. Glaciol.*, *9*, 39–44.

Comiso, J. C., D. J. Cavalieri, and T. Markus (2003), Sea ice concentration, ice temperature, and snow depth using AMSR-E data, *IEEE Trans. Geosci. Remote Sens.*, *41*(2), 243–252.

Grenfell, T. C., J. C. Comiso, M. A. Lange, H. G. Eicken, and M. R. Wensnahan (1994), Passive microwave observations of the Weddell Sea during austral winter and early spring, *J. Geophys. Res.*, *99*, 9,995–10,010.

Jeffries, M. O., and W. F. Weeks (1992), Structural characteristics and the development of sea ice in the western Ross Sea, *Antarct. Sci.*, *5*(1), 63–75.

Kunzi, K., S. Patil, and H. Rott (1982), Snow-cover parameters retrieved from Nimbus-7 Scanning Multichannel Microwave Radiometer (SMMR) data, *IEEE Trans. Geosci. Remote Sens.*, *GE-20*, 452–467.

Kwok, R., H. J. Zwally, and D. Yi (2004), ICESat observations of Arctic sea ice: A first look, *Geophys. Res. Lett.*, *31*, L16401, doi:10.1029/2004GL020309.

Kwok, R., G. F. Cunningham, H. J. Zwally, and D. Yi (2006), ICESat over Arctic sea ice: Interpretation of altimetric and reflectivity profiles, *J. Geophys. Res.*, *111*, C06006, doi:10.1029/2005JC003175.

Lange, M. A., P. Schlosser, S. F. Ackley, P. Wadhams, and G. S. Dieckmann (1990), ^{18}O concentrations in sea ice of the Weddell Sea, Antarctica, *J. Glaciol.*, *36*(124), 315–323.

Long, D. G. (2000), *A QuikSCAT/SeaWinds Sigma-0 Browse Product, Version* 2.0, Brigham Young Univ., Provo, Utah.

Long, D. G., and M. R. Drinkwater (1999), Cryosphere applications of NSCAT data, *IEEE Trans. Geosci. Remote Sens.*, *37*, 1671–1684.

Lucieer, A., and A. Stein (2005), Texture-based landform segmentation of LiDAR imagery, *Int. J. Appl. Earth Obs. Geoinf.*, *6*, 261–270.

Markus, T., and D. J. Cavalieri (1998), Snow depth distribution over sea ice in the Southern Ocean from satellite passive microwave data, in *Antarctic Sea Ice: Physical Processes, Interactions and Variability, Antarct. Res. Ser.*, vol. 74, edited by M. O. Jeffries pp. 19–40, AGU, Washington, D. C.

Markus, T., D. Powell, and J. R. Wang (2006), Sensitivity of passive microwave snow depth retrievals to weather effects and snow evolution, *IEEE Trans. Geosci. Remote Sens.*, *44*, 68–77.

Markus, T., D. J. Cavalieri, A. Gasiewski, M. Klein, J. Maslanik, D. Powell, and M. Sturm (2006), Microwave signatures of snow on sea ice: Observations, *IEEE Trans. Geosci. Remote Sens.*, *44*, 3081–3090.

Maslanik, J. A., et al. (2006), Spatial variability of Barrow-area shore-fast sea ice and its relationships to passive microwave emissivity, *IEEE Trans. Geosci. Remote Sens.*, *44*, 3021–3031.

Massom, R. A., et al. (2001), Snow on Antarctic sea ice, *Rev. Geophys.*, *39*(3), 413–445.

Massom, R. A., et al. (2006), ARISE (Antarctic Remote Ice Sensing Experiment) in the East 2003: Validation of satellite-derived sea ice data products, *Ann. Glaciol.*, *44*, 288–296.

Ojala, T., and M. Pietikäinen (1999), Unsupervised texture segmentation using feature distributions, *Pattern Recognition*, *32*, 477–486.

Ojala, T., M. Pietikäinen, and T. Mäenpää (2002), Multi-resolution grey-scale and rotation invariant texture classification with local binary patterns, *IEEE Trans. Pattern Anal. Machine Intell.*, *24*, 971–987.

Onstott, R. G., (1992), SAR and scatterometer signatures of sea ice, in *Microwave Remote Sensing of Sea Ice, Geophys. Monogr. Ser.*, vol. 68, edited by F. D. Carsey, pp. 73-104, AGU, Washington, D. C.

Powell, D. C., T. Markus, D. J. Cavalieri, A. J. Gasiewski, M. Klein, J. A. Maslanik, J. C. Stroeve, and M. Sturm (2006), Microwave signatures of snow on sea ice: Modeling, *IEEE Trans. Geosci. Remote Sens.*, *44*, 3091–3102.

Stroeve, J. C., T. Markus, J. A. Maslanik, D. J. Cavalieri, A. J. Gasiewski, J. F. Heinrichs, J. Holmgren, D. Perovich, and M. Sturm (2006), Impact of surface roughness on AMSR-E sea ice products, *IEEE Trans. Geosci. Remote Sens.*, *44*, 3103–3117.

Sturm, M., K. Morris, and R. A. Massom (1998), The winter snow cover of the West Antarctic pack ice: Its spatial and temporal variability, in *Antarctic Sea Ice: Physical Processes, Interactions and Variability, Antarct. Res. Ser.*, vol. 74, edited by M. O. Jeffries, pp. 1-18, AGU, Washington, D.C.

Sturm, P., M. Leuenberger, F. L. Valentino, B. Lehmann, and B. Ihly (2006), Measurements of CO_2, its stable isotopes, O_2/N_2, and ^{222}Rn at Bern, Switzerland, *Atmos. Chem. Phys.*, *6/7*, 1991–2004.

Wingham, D., et al. (2006), CryoSat: A mission to determine the fluctuations in Earth's land and marine ice fields, *Adv. Space Res.*, *37*, 841–871.

Worby, A. P., R. A. Massom, I. Allison, V. I. Lytle, P. Heil (1998), East Antarctic sea ice: A review of its structure, properties and drift, in *Antarctic Sea Ice: Physical Processes, Interactions and Variability, Antarct. Res. Ser.*, vol. 74, edited by M. O. Jeffries pp. 41–67, AGU, Washington, D. C.

Worby, A. P., C. Geiger, M. J. Paget, M. van Woert, S. F. Ackley, and T. DeLiberty (2008), The thickness distribution of Antarctic sea ice, *J. Geophys. Res.*, doi:10.1029/2007JC004254, in press.

V. I. Lytle, CliC International Project Office, Norwegian Polar Institute, N-9296, Tromsø, Norway.

T. Markus, NASA Goddard Space Flight Center, Greenbelt, MD 20771, USA.

R. A. Massom, A. D. Steer, and A. P. Worby, Australian Antarctic Division and ACE CRC, Private Bag 80, University of Tasmania, Hobart, Tasmania 7001, Australia. (a.worby@utas.edu.au)